Progress In Electromagnetics Research, Vol. 176, 95–108, 2023

A Novel Optical Proximity Correction (OPC) System Based on Deep Learning Method for the Extreme Ultraviolet (EUV) Lithography

Li-Ye Xiao[1], Jun-Nan Yi[1], Yiqian Mao[2], Xin-Yue Qi[1], Ronghan Hong[1, *], and Qing Huo Liu[1, 3, *]

(*Invited Paper*)

Abstract—As one of the most important technologies for the next generation very-large scale integrated circuit fabrication, extreme ultraviolet (EUV) lithography has attracted more and more attention in recent years. However, in EUV lithography, the optical distortion of the printed image on wafer always has negative impacts on the imaging performance. Thus, to enhance the imaging performance of EUV system, especially for small critical dimensions, in this work, a novel optical proximity correction (OPC) system based on the deep learning technique is proposed. It includes a forward module and an inverse module, where the forward module is employed to fast and accurately map the mask to the corresponding near field of the plane above the stack to help the construction of training dataset for the inverse module operation, and the inverse module is employed to fast and accurately map the target printed image to the corrected mask. Numerical examples demonstrate that compared with traditional full-wave simulation, the forward module can greatly improve the computational efficiency including the required runtime and memory. Meanwhile, different from time consuming iterative OPC methods, the corrected mask can be immediately obtained as the target printed image is input using the trained inverse module.

1. INTRODUCTION

In recent years, as the most advanced lithography technology after deep ultraviolet (DUV) lithography, extreme ultraviolet (EUV) lithography at 13.5 nm illumination wavelength has attracted more and more attention as the critical dimension of integrated circuits shrinks below 22 nm [1]. However, inevitably, the imaging performance of lithography systems is negatively affected by optical proximity effect and mask shadowing effects [2–5].

Fortunately, more and more optical proximity correction (OPC) methods have been proposed to improve the equality of printed image for lithography systems. Through pre-warping the masks, OPC can compensate for imaging distortions to converge to the target patterns. Usually, OPC approaches can be classified into rule-based OPC and model-based OPC [2].

Rule-based OPC can be simply implemented, but at the technology nodes below 90 nm for DUV lithography, rule-based OPC cannot be effective. Different from rule-based OPC, model-based OPC is based on the physical and mathematical models of the OPC framework to find the global optimal solution, thus, it can achieve smaller lithographic resolution limitation [6, 7].

Further, model-based OPC can be classified into edge-based OPC (EBOPC) and pixel-based OPC (PBOPC). In respect of working principle, EBOPC separates the edges of mask into several fragments and nudges them to find the optimal solutions, while PBOPC decomposes the mask into pixels and

Received 16 October 2022, Accepted 20 December 2022, Scheduled 8 January 2023

* Corresponding author: Ronghan Hong (ronghanhong@xmu.edu.cn), Qing Huo Liu (qhliu@eias.ac.cn).

[1] Institute of Electromagnetics and Acoustics, Xiamen University, Xiamen 361005, China. [2] Department of Electrical and Computer Engineering, Duke University, Durham, NC 27708, USA. [3] Eastern Institute for Advanced Study, Ningbo 315200, China.

optimizes their binary values [6]. Compared with EBOPC, PBOPC has higher optimization freedom, so it is applicable to the nodes below 45 nm for both DUV and EUV lithography [7, 8]. To sum up, a series of PBOPC approaches have been developed to follow the process variations of advanced lithography systems in recent years [9–15].

However, due to the repeated calls to the lithography simulation and mask-imaging correction program [16], model-based OPC will consume lots of CPU time during iterations [6]. To reduce high-computational complexity of this process, machine learning techniques have been applied in OPC [17–19]. Compared with traditional computational methods, the machine learning-based methods usually have higher computational efficiency after training [20–22].

The main idea of machine learning-based methods is to build a mapping relationship by training a neural network model based on the optical diffraction physics. Once a new input is entered into the trained neural network model, the corresponding output can be immediately obtained. For examples, [21] introduces basic machine learning-based OPC with support vector machine and neural networks. Through discussing learning parameters and preparation of compact learning data set, a guidance technique is proposed to avoid the over-fitting problem. In [23], a neural network classifier-based OPC is proposed, where a neural network classifier serves as a mask bias model. Compared to state-of-the-art machine learning-OPC with regression methods, the proposed OPC method reduces the prediction error of mask bias and training time by 29% and 80%, respectively. To reduce the runtime of PBOPC and complexity of mask, a machine learning-based OPC model is proposed in [24] and tested on both Metal and Poly layers at 45 nm technology node. The simulation results illustrate that the proposed model can effectively reduce the runtime of the PBOPC software and improve the mask manufacturability at the cost of acceptable image fidelity degradation. These kinds of machine learning based-OPC methods require the approximate algorithm or the full-wave simulation to collect the training dataset. However, for the approximate algorithm, it is hard to achieve good results with a small critical dimension. Meanwhile, the full-wave simulation requires large computational cost for large electrical dimensions, and the computational cost will be too large to realize.

To further enhance the performance of OPC including computational efficiency and accuracy, in this work, an OPC system based on deep learning is proposed with a new angle for the EUV lithography, especially for the small critical dimension. Different from PBOPC or EBOPC, the proposed OPC system includes a forward module and an inverse module, where the forward module is employed to fast and accurately map the mask to the corresponding near field of the plane above the stack instead of full-wave simulation to enhance the modeling efficiency, and the inverse module is employed to fast and accurately map the target printed image to the corrected mask. To accurately map the mask to the corresponding near field distribution for the small critical dimension, two connected U-Nets are employed to construct the forward module, where the first U-Net is employed to map the binary mask to the preliminary field distributions on the wafer, and the second U-Net is employed to further enhance the mapping accuracy of the printed image. Due to the fast-computational efficiency of machine learning technique, the forward module instead of full-wave simulation can greatly improve computational efficiency to help the construction of training dataset for the inverse module operation. Meanwhile, once the inverse module is well trained, it can immediately obtain the corrected mask after the target printed image is input.

Compared with other OPC approaches, the main contributions of the proposed OPC system can be summarized as follows: first, a forward module with strong mapping ability and good mapping performance which maps the mask to the corresponding near field of the plane above the stack is proposed to match up with the inverse module to greatly enhance the modeling efficiency. Especially, compared with spectral-element spectral-integral (SESI) method [25] which is an advanced computational algorithm for doubly periodic structures in layered media, the forward module can greatly reduce the computational cost. Second, both forward and inverse modules can produce very large-scale patterns with small computational costs in the required CPU time and computer memory, compared with SESI and other OPC algorithms [1]. Third, for the small critical dimension, which is a well-known challenge in EUV lithography, both forward and inverse modules have excellent performance, i.e., the forward module can fast and accurately output the corresponding near field distribution, and the proposed inverse module can rapidly produce a corrected mask to improve the quality of printed image on wafer.

This work is organized as follows. In Section 2, the background of the problem is briefly described. In Section 3, the proposed OPC system, including the forward and inverse modules, is discussed in detail. In Section 4, the numerical results for both forward and inverse modules are exhibited. Finally, we summarize this work in Section 5.

2. PROBLEM STATEMENT

As shown in Fig. 1, the EUV structure consists of a mask stack and a multilayer Bragg reflector stack, and the 6-degree incident plane wave is selected as the EUV light rays. The mask stack contains a mask patterns above the multilayer Bragg reflector stack consisting of 40 Si-Mo bilayers to effectively reflect energy of the 13.5-nm plane wave at 6-degree incidence. Meanwhile, the mask region is covered by absorbers to absorb most of EUV light, while the mask regions without absorbers will reflect most of the EUV light into the projector optics. The corresponding electrical parameters of the above-mentioned materials are also shown in Fig. 1. The projector optics is used to project the layout pattern from the mask onto the wafer. After the development of photoresist, the layout pattern will be printed on the wafer.

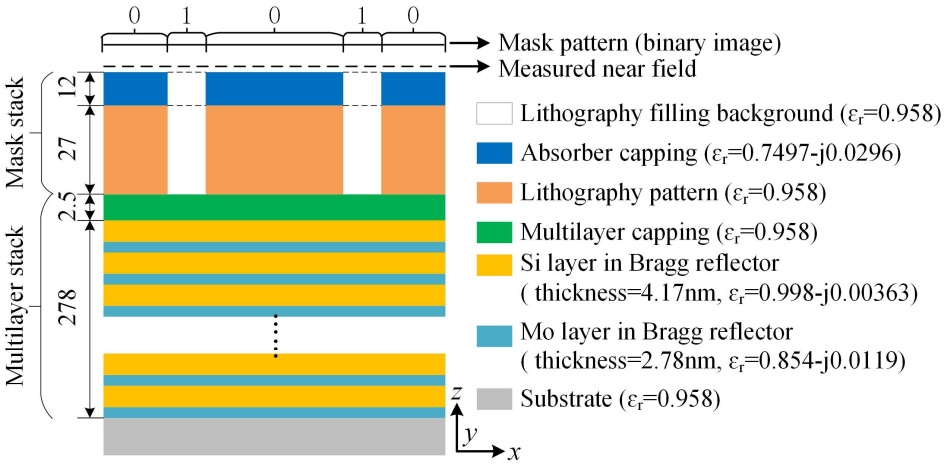

Figure 1. The unit-cell of the EUV structure, which consists of a mask stack and a multilayer Bragg reflector stack. The 6-degree incident plane wave is selected as the EUV light rays.

3. PROPOSED MODEL

In our OPC system, the input of the forward module is the mask pattern which is a binary image, and the output is the near or far field on the plane above the mask stack. For the inverse module, the desired print image is set as the input and the corresponding corrected mask set as the output. After the training process, the forward module is expected to immediately output the corresponding near field distribution once the mask image is input, and the inverse module is expected to output the corrected mask once the desired printed image on wafer is input. Due to the fast-computational efficiency of machine learning technique, the forward module instead of full-wave simulation can greatly improve computational efficiency to help the construction of training dataset for the inverse module operation.

3.1. Forward Module

To replace the time-consuming full-wave simulation in the OPC process, the deep learning technique with higher computational efficiency is employed. Meanwhile, it is well known that with the critical dimension decreasing, the optical scattering process is more and more complex. To accurately map the relationship between the mask and the corresponding near field, here the forward module is constructed

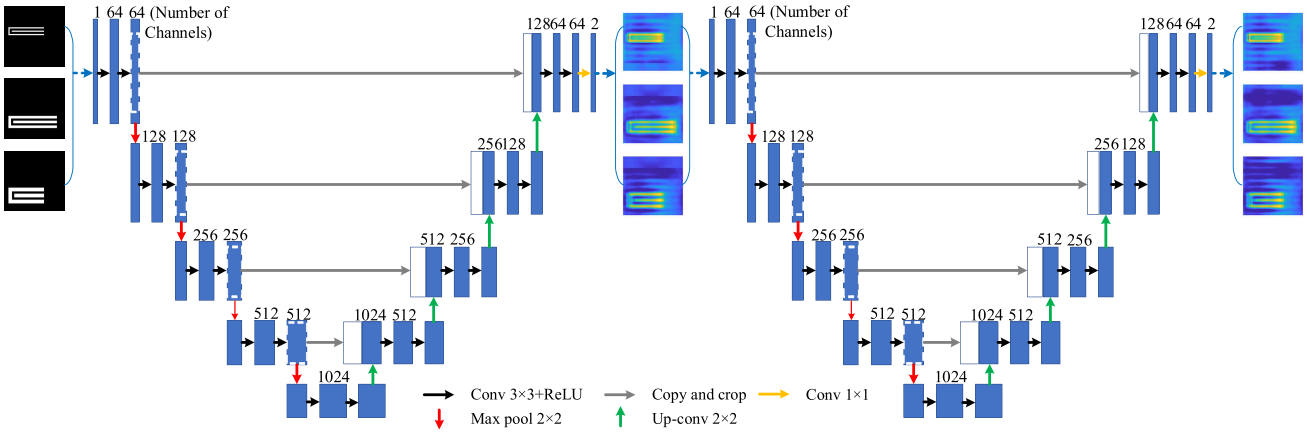

Figure 2. The structure of the proposed forward module with two connected U-Nets, where the first U-Net inputs the binary mask and outputs the preliminary near field distribution to further input to the second U-Net for obtaining the final near field distribution.

with two connected U-Nets, where the first U-Net is input with the binary mask and outputs the preliminary field distribution, then the obtained image is input to the second U-Net to obtain the final near field distribution. The second U-Net here is employed to further enhance the mapping accuracy. One should note the training, validation, and testing data toned to be normalized to the range of [0, 1] before they are input to the machine model, and the mask value is presented with the binary value 0 and 1.

U-Net, which is first proposed for biomedical image segmentation [26], is a classifier for the pixel-wise problem. U-Net consists of a contracting path and an expansive path. Both these paths have repeated application of 3×3 convolutions, batch normalization, and rectified linear unit (ReLU), but a 2×2 max pooling in the contracting path is replaced by a 3×3 up convolution in the expansive path. The input image goes through the convolution layers and average pooling layers to extract local scale features and global scale features, and then to the transposed convolution layers to restore the input size. Short connections between the down-sampling path and up-sampling path can help combine previous information to the output and speed up the training convergence. The structure of forward module consisting of two connected U-Nets is shown in Fig. 2. The training samples for the forward module are constructed on the basis of following cases shown in Fig. 3 which elaborates nine categories of simple mask patterns covering a wide range of local combinations. The choice of training patterns is important for the accuracy of the model. The more local combinations are covered, the more accurate the model will be [21]. Samples (a)–(h) are employed to train, while Sample (i) is employed to validation, and the corresponding variables are set in the following Table 1.

3.2. Inverse Module

For the inverse module, the desired print image is set as the input and the corresponding corrected mask set as the output. However, how to construct the desired training dataset before the training process is the key point of the inverse module. Thus, we build an OPC model which contains two steps. Take a rectangle as an example as shown in Figs. 4(a)–(c). The first step is to expand the original domain with the increasement of m_1 and m_2 in two directions, respectively. Then, the four sides are concaved/bulged with their middle points moving inward by the lengths of h_1, h_2, h_3, and h_4, respectively. If the width of one side is smaller than $w_{\text{threshold}}$, then the corresponding adjacent side is bulged. $w_{\text{threshold}}$ here is a threshold to decide whether to concave or bulge a side. In this work, the $w_{\text{threshold}}$ for the rectangle is set as 3 nm. As shown in Fig. 4(d), if L_3 is smaller than $w_{\text{threshold}}$, then the corresponding adjacent sides are bulged with h_5 and h_7, as shown in Fig. 4(f), after the domain is expanded with increasement of m_3 and m_4 in two directions, respectively. On the contrary, if the length of a side is larger than $w_{\text{threshold}}$, then the corresponding side is concaved, as shown in Fig. 4(c). As shown in Fig. 4(g), if L_5 is larger than $w_{\text{threshold}}$, then the corresponding adjacent sides are concaved with h_9 and h_{11}, as shown in

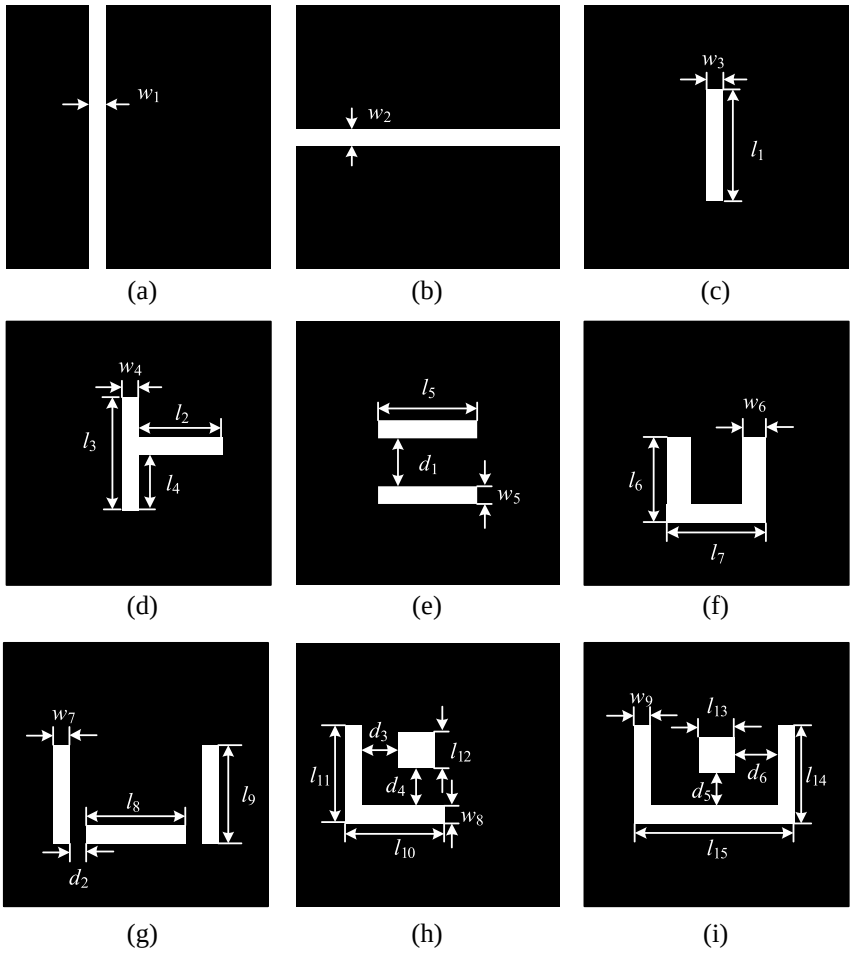

Figure 3. Mask patterns used for training and testing of the proposed forward module, where patterns (a)–(h) are employed for training and pattern (i) is employed for testing.

Fig. 4(i), after the domain is expanded with increasement of m_5 and m_6 in two directions, respectively.

Then the obtained masks are input to the trained forward module, and the corresponding printed image on wafer can be immediately obtained. To characterize the deviation between the printed image and the original desired printed image (target), the relative pattern error is defined as

$$\mathrm{Err}_{\mathrm{pattern}} = \frac{\|\mathbf{m}_P - \mathbf{m}_T\|}{\|\mathbf{m}_T\|} \tag{1}$$

where $\mathbf{m}_P$ is the matrix of the predicted binary image, and $\mathbf{m}_T$ is the matrix of the desired binary image. The samples with small relative pattern errors are selected to construct a training dataset for the inverse module.

Meanwhile, the inverse module is also constructed on the basis of U-Net. Its structure is shown in Fig. 5, where the blue box represents the multi-channel images, and its height and width indicate the size of image and number of channels (also marked in blue on top of the boxes), respectively. The operations are represented by different colors and orientation arrows. Based on this architecture, the input single-channel binary image can be converted into the output single-channel binary image.

4. NUMERICAL RESULTS

In this work, all the computations are performed on a workstation with an Intel i9-10940X 3.30 GHz CPU, 256 GB RAM and NVIDIA GeForce RTX 3090 GPU. The training samples for the forward module

Table 1. Parameters distribution for the mask patterns in Fig. 3 (unit: nm).

Parameter	w_1	w_2	w_3	w_4	w_5	w_6	w_7	w_8
Mini. value	2	2	2	2	2	2	2	2
Maxi. value	8	8	8	8	8	8	8	8
Step	1	1	1	1	1	1	1	1
Parameter	w_9	l_1	l_2	l_3	l_4	l_5	l_6	l_7
Mini. value	2	4	4	4	4	4	4	4
Maxi. value	8	60	60	60	60	60	60	60
Step	1	4	4	4	4	4	4	4
Parameter	l_8	l_9	l_{10}	l_{11}	l_{12}	l_{13}	l_{14}	l_{15}
Mini. value	4	4	4	4	2	2	4	4
Maxi. value	60	60	60	60	10	10	60	60
Step	4	4	4	4	2	2	4	4
Parameter	d_1	d_2	d_3	d_4	d_5	d_6		
Mini. value	2	0	2	2	2	2		
Maxi. value	20	10	20	20	20	20		
Step	2	2	2	2	2	2		

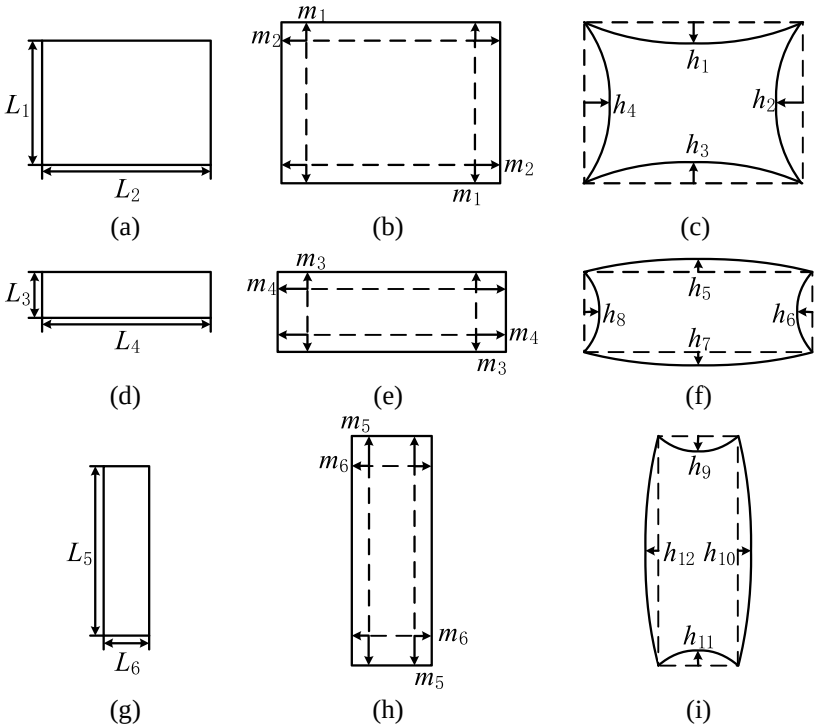

Figure 4. The proposed OPC model for the training sample generation for the inverse module. (b), (e) and (h) are the first step to expand the domain of the original one shown in (a), (d) and (g), respectively. (c), (f) and (i) present that the middle points of the four sides are concaved/bulged.

are generated with Wavenology EM software [27] developed by Wave Computation Technologies, where the spectral-element spectral-integral (SESI) method [25] is employed and suitable for this problem.

4.1. Experimental Setups

The forward module consists of 320 samples. Samples (a)–(h) contain 40 samples, respectively, for training, and 40 samples, namely Sample (i) for the validation. The training samples have the mask dimensions of 128 nm × 128 nm, and they are discretized into 256 × 256 pixels, each pixel having the dimensions of 0.5 nm × 0.5 nm. The near field on the plane 1 nm above the mask stack is set as the output of the forward module. The epoch number is 2000 for both connected U-Nets, and their learning rates are 1×10^{-4} and 5×10^{-5}, respectively. Meanwhile, the mean square error (MSE) is defined as the loss function for the both U-Nets. For the inverse module, totally 400 samples are selected for training, and the other 50 testing samples are employed for validation. Loss function convergence during training process is also recorded in Fig. 6. The training samples for the inverse module also have the dimensions of 128 nm × 128 nm and are discretized into 256 × 256 pixels.

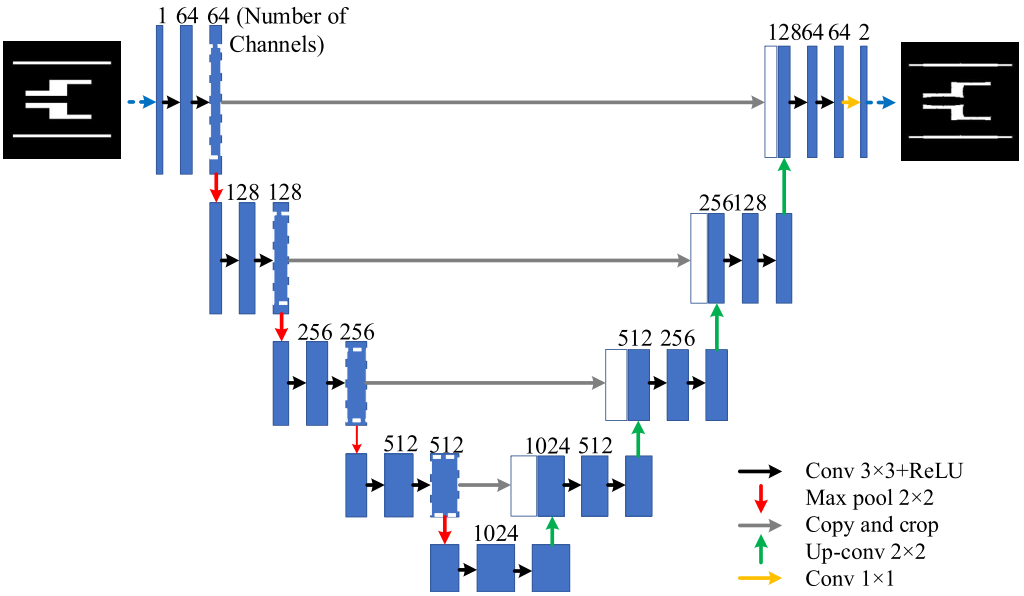

Figure 5. The structure of the inverse module. Its input is the desired printed image on the wafer and the corresponding output is the corrected mask.

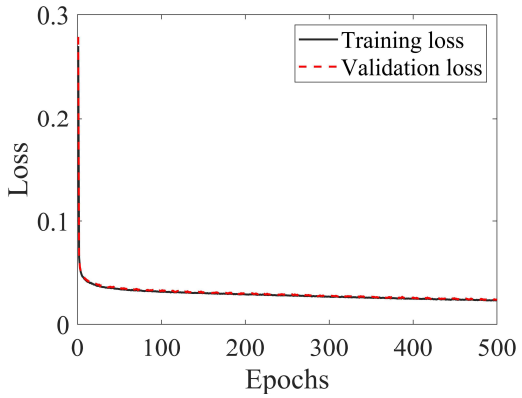

Figure 6. Loss function convergence during training process of the inverse module.

4.2. Forward Module

The forward module is first tested with five different samples which never appear in the training dataset. These five samples have the dimensions of 128 nm × 128 nm, and their near field distributions obtained from SESI are employed to validate the proposed forward module. The misfit between the near field

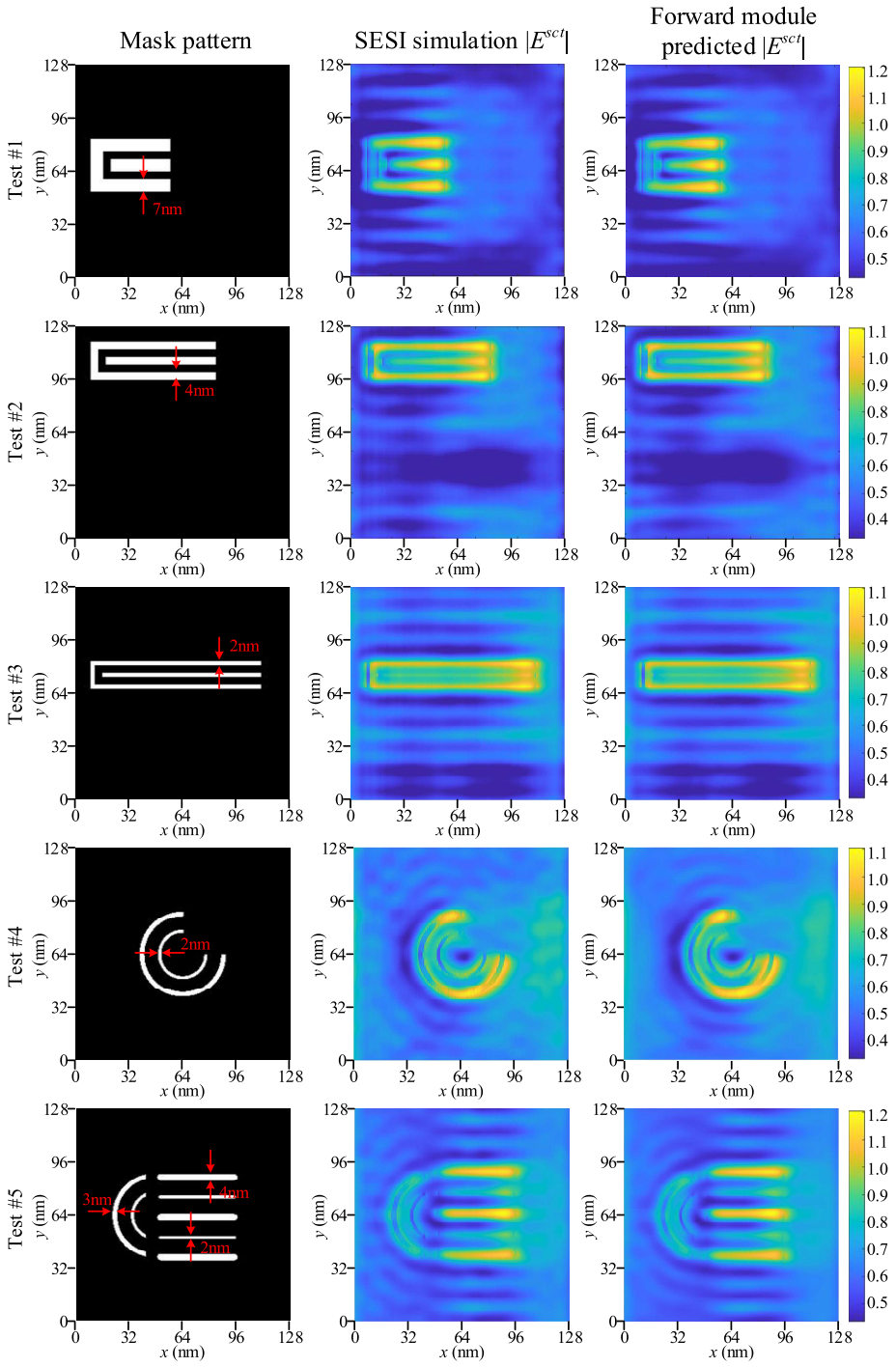

Figure 7. Five different tests are used to evaluate the proposed forward module. The 1st column is the mask pattern with different critical dimensions, the second column is the $|E^{sct}|$ obtained from SESI and the third column is the $|E^{sct}|$ obtained from the forward module.

distributions obtained from SESI and the proposed module is defined as

$$\mathrm{Err}_{\mathrm{data}} = \frac{\|\mathbf{d}_P - \mathbf{d}_T\|}{\|\mathbf{d}_T\|} \tag{2}$$

where $\mathbf{d}_P$ is the matrix of the predicted field distribution, and $\mathbf{d}_T$ is the matrix of the labled field distribution.

The masks of Tests #1–5 are shown in Fig. 7, where Tests #1–3 are based on Sample (i) shown in Fig. 3, and the critical dimension of Tests #1, #2, and #3 gradually decreases from 7 nm to 2 nm. Meanwhile, unlike the training samples which are constructed with straight lines. Test #4 has a totally different shape as it is constructed with two curves, and its minimum critical dimension is 2 nm. Test #5 is mixed with straight lines and curves, while the widths of lines include 2 nm, 3 nm, and 4 nm. The misfits of $|E^{sct}|$ obtained from SESI and the proposed model from Tests #1 to #5 are listed in Table 2. It can be seen that even though Tests #1–3 have different critical dimensions, their misfits are at the same level. For Test #4, when the mask contains a curved pattern, compared with the SESI results, the proposed forward module can also obtain a desired accuracy. Meanwhile, the results from Tests #1–4 have the same accuracy level, even though Tests #1–3 are constructed with straight lines. Test #5 is mixed with different types of mask and critical dimensions, and its misfits of $|E^{sct}|$ obtained from SESI and the proposed model still maintain a stable accuracy level (less than 4.2%) as the other test samples.

Table 2. Misfits of $|E^{sct}|$ obtained from SESI the proposed model.

	Test #1	Test #2	Test #3	Test #4	Test #5
Misfit	0.0431	0.0395	0.0374	0.0416	0.0422

It can be concluded that the proposed forward module can accurately map the mask pattern to the corresponding near field not only with different critical dimensions, but also with different pattern types. Then a very large mask pattern is employed to further evaluate the proposed forward module. As shown in Fig. 8, the mask has the dimensions of 6400 nm × 6400 nm, corresponding to electrical dimensions of about $474\lambda \times 474\lambda$, and the predicted near field is shown in Fig. 8.

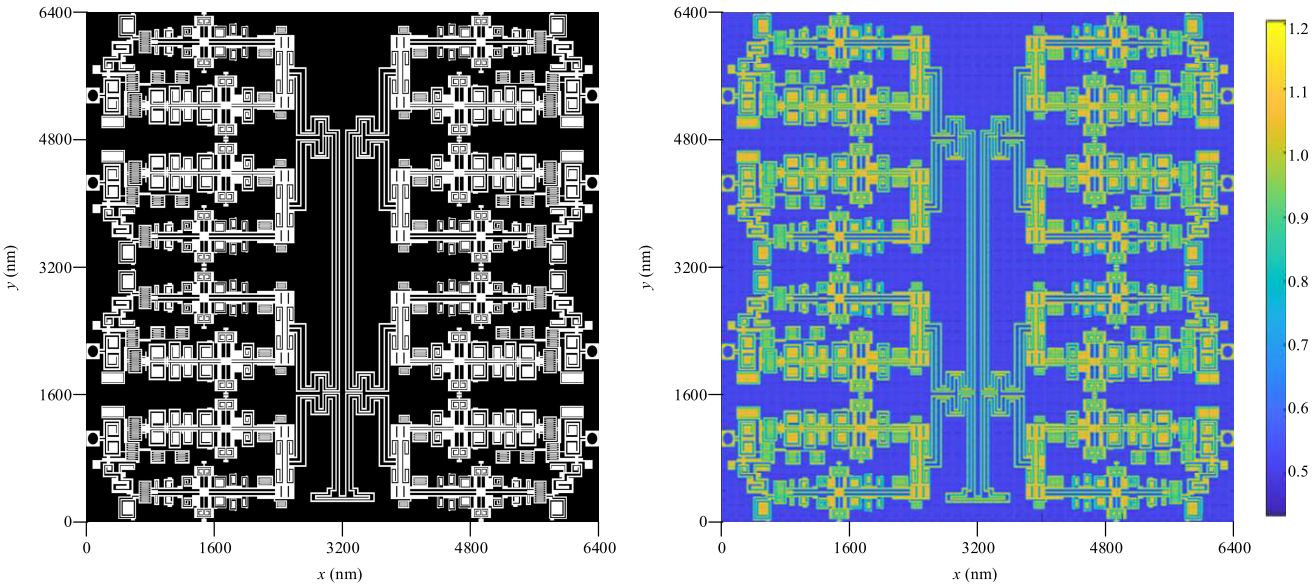

Figure 8. A very large mask pattern of dimensions 6400 nm × 6400 nm is employed to evaluate the proposed forward module. Left: the mask pattern. Right: the corresponding $|E^{sct}|$ obtained from the forward module.

Table 3. Comparison of SESI and proposed forward module.

		Test #1	Test #2	Test #3
Size (nm)		128 × 128	128 × 128	128 × 128
Running time	SESI	62 min	68 min	69 min
	Forward module	64 ms	64 ms	64 ms
Memory	SESI	212 GB	223 GB	229 GB
	Forward module	0.42 GB	0.42 GB	0.42 GB
		Test #4	Test #5	Test #6
Size (nm)		128 × 128	128 × 128	6400 × 6400
Running time	SESI	79 min	83 min	125 days*
	Forward module	64 ms	64 ms	102 s
Memory	SESI	232 GB	237 GB	560 TB*
	Forward module	0.42 GB	0.42 GB	9.8 GB

* These are estimated costs, due to the limitation of computation resources for the full-wave solution.

Meanwhile, the CPU time and required computer memory are also recorded in Table 3 to evaluate the computational efficiency of the proposed forward module. It can be seen that the proposed forward module is largely superior to SESI in the respects of CPU time and required memory, even though the proposed forward module required extra GPU computations. Meanwhile, it should be noted that in [21], SESI has been confirmed to have higher computational efficiency than SEBI (spectral-element boundary-integral) and commercial software COMSOL for doubly periodic structures in layered media. Thus, the proposed forward module has reliable and efficient mapping ability between the mask and the corresponding near field distribution.

4.3. Inverse Module

For the inverse module, four samples which never appear in the training dataset are employed to evaluate the performance of the proposed inverse module. These four samples have the dimensions of 128 nm × 128 nm, and the predicted masks obtained from the inverse module are input to SESI and the forward module to compute corresponding field distributions.

With the critical dimension decreasing, it is a huge challenge for the imaging performance of optical lithography systems. The critical dimensions of Tests #7–10 are 4 nm, 9 nm, 4 nm, and 2.5 nm, and the corresponding electrical dimensions are 0.3λ, 0.52λ, 0.3λ, and 0.19λ, respectively. The targets of Tests #7–10 are shown in Fig. 9, where Tests #7–9 are on the basis of Samples (i), (e), and (h), respectively, and Test #10 is totally different from the training samples. The relative pattern errors, as defined in Eq. (1), between the target and printed image on the wafer of Test #7–10 are listed in Table 4, where Misfit_1 is the misfit between the printed image with the forward module and the corresponding target, and Misfit_2 is the misfit between the printed image with SESI and the corresponding target. In [1], different SMO (source mask optimization) algorithms in the aspects of image performance are evaluated and compared, based on the simulations of 22 nm and 16 nm layouts. It could be seen for the critical dimensions of 22 nm and 16 nm that the runtime of SMO algorithms is more than 8000 s. Thus, the proposed inverse module is much more efficient especially for smaller critical dimension.

For comparison, the original targets are set as the masks, and the corresponding printed images obtained from SESI are also provided in Fig. 9. The relative pattern errors between the targets and printed images are listed in Table 4, i.e., Misfit_3. It can be seen that the masks provided by the proposed inverse module can obtain smaller misfits than the original target as the mask.

Then a large pattern is also employed to evaluate the proposed inverse module. As shown in Fig. 10, the target has the dimension of 6400 nm × 6400 nm, and the predicted mask is shown in Fig. 10. Meanwhile, the CPU time and required computational memory are also recorded in Table 5. Different from the traditional iterative method, it can be seen that the proposed inverse module, which can

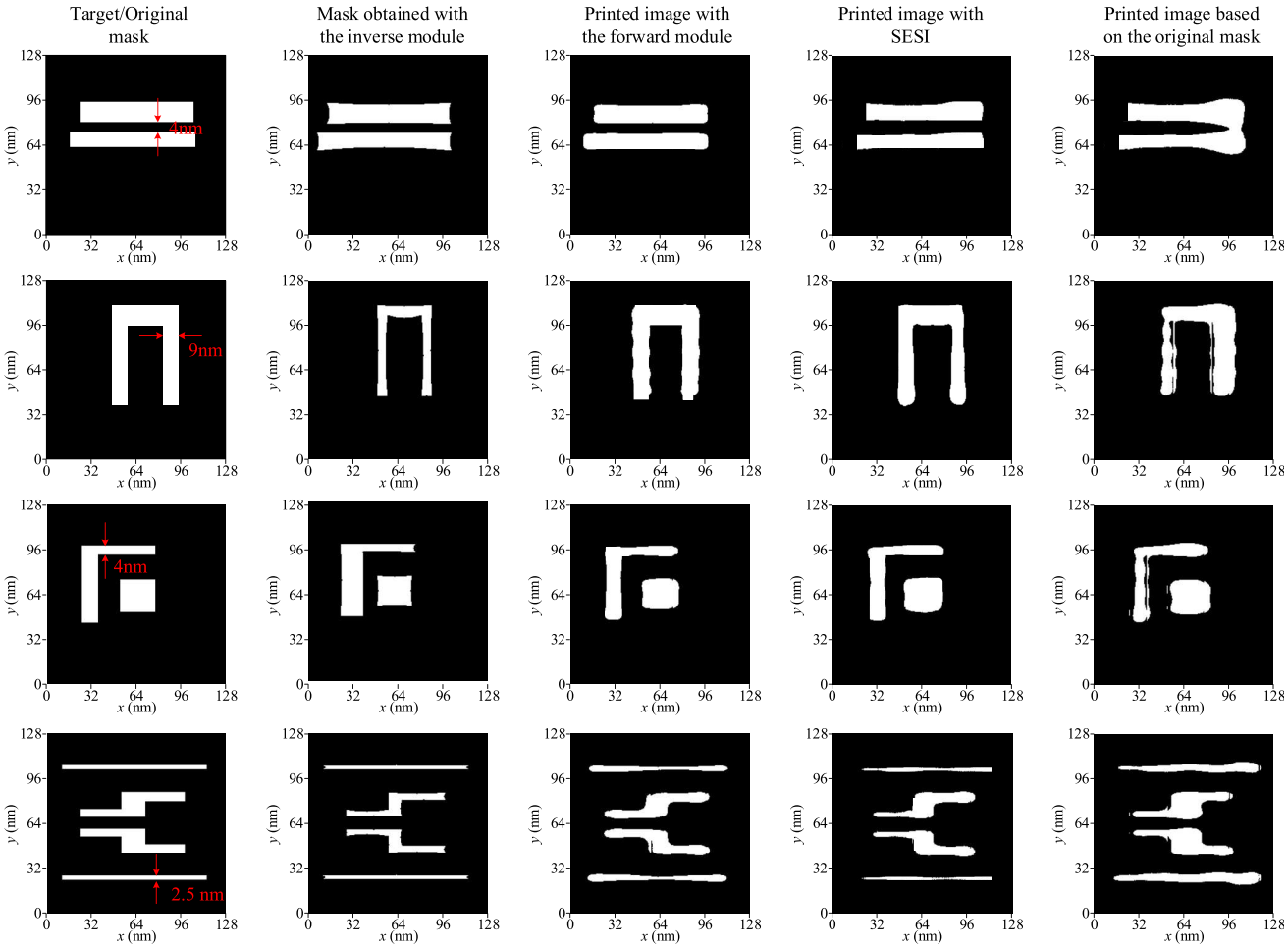

Figure 9. Four different tests are used to evaluate the proposed inverse module. The 1st column presents the targets (the original masks); the 2nd column presents the corrected masks obtained from the proposed inverse module; the 3rd column presents the printed image obtained from the forward module with the corrected masks; and the 4th and 5th columns present the printed images obtained from SESI with the corrected masks and original masks.

Table 4. Misfits of printed image and the corresponding target.

	Test #7	Test #8	Test #9	Test #10
Misfit_1	0.0632	0.0721	0.0757	0.0948
Misfit_2	0.0698	0.0682	0.0762	0.0872
Misfit_3	0.1342	0.1698	0.1593	0.1839

directly output the corrected mask, has high computational efficiency for different targets, even though extra GPU computations are needed.

As shown in Figs. 9–10 and Tables 4–5, the imaging equality is enhanced with the validation of Tests #7–10. Meanwhile, the computation of the large pattern further verifies the computational efficiency. Thus, the proposed inverse module can be regarded as an effective OPC tool for EUV, especially for small critical dimensions.

Table 5. Running time and required memory of the proposed inverse module.

	Size	Running time	Memory
Test #7	128 nm × 128 nm	32 ms	0.42 GB
Test #8	128 nm × 128 nm	32 ms	0.42 GB
Test #9	128 nm × 128 nm	32 ms	0.42 GB
Test #10	128 nm × 128 nm	32 ms	0.42 GB
Test #11	6400 nm × 6400 nm	51 s	9.8 GB

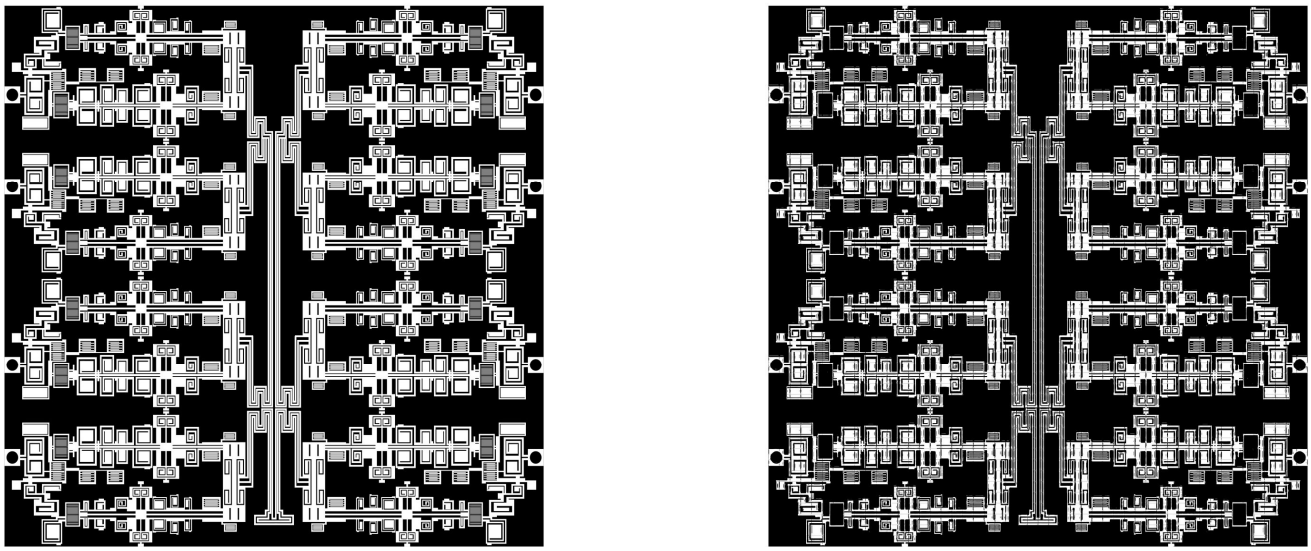

Figure 10. A very large mask pattern of dimensions 6400 nm × 6400 nm is employed to evaluate the proposed inverse module. Left: the target pattern. Right: the corresponding predicted mask obtained from the inverse module.

5. CONCLUSION

To enhance the imaging performance of EUV system, especially for critical dimensions smaller than 3 nm, a novel optical proximity correction (OPC) system based on the deep learning technique is proposed in this work. It includes a forward module and an inverse module. The forward module is employed to map the mask to the corresponding near field on a plane above the stack, and the inverse module is employed to map the target printed image to the corrected mask.

First, the proposed forward module is tested with different types and scales of samples. Compared with full-wave simulations such as the SESI method, the misfit between the near field distributions obtained from SESI and the proposed module is about 4%. It can be concluded that the proposed forward module can accurately map the mask pattern to the corresponding near field not only with different critical dimensions, but also with different pattern types. Meanwhile, compared with SESI, the forward module has largely improved the computational efficiency including the required CPU time and memory by a factor of 540 and 6769, respectively. Then, the inverse module is constructed and evaluated with different scales and types of samples. It can be seen that different from the traditional iterative method, the proposed inverse module can directly output the corrected mask with high computational efficiency. Meanwhile, compared with the original mask, the corrected mask can enhance the imaging equality by a factor of 2 according to the misfit between the printed image and target, especially for the critical dimensions smaller than 3 nm.

Therefore, the proposed OPC system, including the forward module and inverse module, can be regarded as a reliable and effective OPC tool for EUV systems, especially for small critical dimensions. In the future, we will work on OPC for a larger mask pattern with smaller critical dimensions; meanwhile, how to further reduce the training cost of the machine learning based-OPC method is also a necessary point to study.

ACKNOWLEDGMENT

This research was funded by Science and Technology Projects of Innovation Laboratory for Sciences and Technologies of Energy Materials of Fujian Province (IKKEM) under Grant HRTP-[2022]-32, and in part by the National Natural Science Foundation of China under Grant 62001406 and Grant 61471105.

REFERENCES

1. Ma, X., Z. Wang, X. Chen, Y. Li, and G. R. Arce, "Gradient-based source mask optimization for extreme ultraviolet lithography," *IEEE Trans. Comput. Imag.*, Vol. 5, No. 1, Mar. 2019.
2. Erdmann, A., P. Evanschitzky, F. Shao, T. Fühner, G. F. Lorusso, E. Hendrickx, M. Goethals, R. Jonckheere, T. Bret, and T. Hofmann, "Predictive modeling for EUV-lithography: The role of mask, optics, and photoresist effects," *Proc. SPIE*, Vol. 8171, No. 37, 23–33, Oct. 2011.
3. Cain, J., P. Naulleau, and C. Spanos, "Modeling of EUV photoresists witha resist point spread function," *Proc. SPIE*, Vol. 5751, 1101–1109, 2005.
4. Ma, X., J. Wang, X. Chen, Y. Li, and G. R. Arce, "Gradient-based inverseextreme ultraviolet lithography," *Appl. Opt.*, Vol. 54, No. 24, 7284–300, Aug. 2015.
5. Song, H., L. Zavyalova, I. Su, J. Shiely, and T. Schmoeller, "Shadowing effect modeling and compensation for EUV lithography," *Proc. SPIE*, Vol. 7969, No. 79691O, 2011.
6. Ma, X. and G. R. Arce, *Computational Lithography*, 1st Edition, Wiley Series in Pure and Applied Optics, John Wiley and Sons, New York, 2010.
7. Poonawala, A. and P. Milanfar, "Double-exposure mask synthesis using inverse lithography," *Journal of Microlithography Microfabrication & Microsystems*, Vol. 6, No. 4, 241–246, 2007.
8. Cobb, N. and D. Dudau, "Dense OPC and verification for 45 nm," *Proc. SPIE*, Vol. 6154, No. 61540I, Mar. 2006.
9. Sherif, S., B. Saleh, and R. Leone, "Binary image synthesis using mixed integer programming," *IEEE Trans. on Image Proc.*, Vol. 4, 1252–1257, 1995.
10. Liu, Y. and A. Zakhor, "Binary and phase shifting mask design for optical lithography," *IEEE Trans. Semicond. Manuf.*, Vol. 5, No. 2, 138–152, 1992.
11. Granik, Y., "Solving inverse problems of optical microlithography," *Proc. SPIE*, Vol. 5754, 506–526, 2004.
12. Granik, Y., "Fast pixel-based mask optimization for inverse lithography," *J. Microlith. Microfab. Microsyst.*, Vol. 5, No. 4, 043002, 2006.
13. Jia, N., A. K. Wong, and E. Y. Lam, "Robust mask design with defocus variation using inverse synthesis," *Proc. SPIE, Lithography Asia*, Vol. 7714, No. 71401W, 2008.
14. Shen, Y., N. Jia, N. Wong, and E. Y. Lam, "Robust level-set-based inverse lithography," *Opt. Express*, Vol. 19, No. 6, 5511–5521, 2011.
15. Shen, Y., N. Wong, and E. Y. Lam, "Aberration-aware robust mask design with level-set-based inverse lithography," *Proc. SPIE*, Vol. 7748, No. 77481U, 2010.
16. Wong, A. K., *Resolution Enhancement Techniques in Optical Lithography*, SPIE Press, 2001.
17. Frye, R., E. Rietman, and K. Cummings, "Neural network proximity effect corrections for electron beam lithography," *IEEE International Conference on Systems, Man and Cybernetics Conference Proceedings*, 704–706, 1990.
18. Jedrasik, P., "Neural networks application for OPC (optical proximity correction) in mask making," *Microelectron. Eng.*, Vol. 30, 1–4, 1996.

19. Huang, W. C., C. M. Lai, B. Luo, C. K. Tsai, M. H. Chih, C. W. Lai, C. C. Kuo, R. G. Liu, and H. T. Lin, "Intelligent model-based OPC," *Proc. SPIE*, Vol. 6154, 1065–1073, 2006.
20. Zeng, N., P. Wu, Z. Wang, H. Li, W. Liu, and X. Liu, "A small-sized object detection oriented multi-scale feature fusion approach with application to defect detection," *IEEE Trans. Instrum. Meas.*, Vol. 71, Article No. 3507014, 2022.
21. Mao, Y., Q. Zhan, R. Zhang, D. Wang, W.-F. Huang, and Q. H. Liu, "Fast simulation of electromagnetic fields in doubly periodic structures with a deep fully convolutional network," *IEEE Trans. Antennas Propag.*, Vol. 69, No. 5, 2921–2928, 2021.
22. Shim, S., S. Choi, and Y. Shin, "Machine learning (ML)-based lithography optimizations," *2016 IEEE Asia Pacific Conference on Circuits and Systems (APCCAS)*, Jeju, South Korea, 2016.
23. Park, J. W., A. Torres, and X. Song, "Litho-Aware machine learning for hotspot detection," *IEEE Trans. on Comp.-Aided Design of Integrated Circuits and Systems*, Vol. 37, No. 7, 1510–1514, Jul. 2018.
24. Ma, X., S. Jiang, J. Wang, B. Wu, Z. Song, and Y. Li, "A fast and manufacture-friendly optical proximity correction based on machine learning," *Microelectron. Eng.*, Vol. 168, 15–26, 2017.
25. Mao, Y., J. Niu, Q. Zhan, R. Zhang, W.-F. Huang, and Q. H. Liu, "Calderón preconditioned spectral-element spectral-integral method for doubly periodic structures in layered media," *IEEE Trans. Antennas Propag.*, Vol. 68, No. 7, 5524–5533, Jul. 2020.
26. Ronneberger, O., P. Fischer, and T. Brox, "U-net: Convolutional networks for biomedical image segmentation," *International Conference on Medical Image Computing and Computer-assisted Intervention*, 234–241, Springer, 2015.
27. http://www.wavenology.com/?page_id=66.